Distributions of transverse energy and forward energy in ^{16}O- and ^{32}S-induced heavy ion collisions at 60A and 200A GeV

R. Albrecht,[1] T. C. Awes,[2] C. Baktash,[2] P. Beckmann,[3] F. Berger,[3] R. Bock,[1] G. Claesson,[4] G. Clewing,[3] L. Dragon,[3] A. Eklund,[4] R. L. Ferguson,[2] A. Franz,[5,6],* S. Garpman,[4] R. Glasow,[3] H. A. Gustafsson,[4] H. H. Gutbrod,[1] J. Idh,[4] P. Jacobs,[5] K.-H. Kampert,[3] B. W. Kolb,[1] P. Kristiansson,[4] I. Y. Lee,[2] H. Loehner,[3],† I. Lund,[1],† F. E. Obenshain,[2] A. Oskarsson,[4] I. Otterlund,[4] T. Peitzmann,[3] S. Persson,[4] F. Plasil,[2] A. M. Poskanzer,[5] M. Purschke,[3] H.-G. Ritter,[5] S. Saini,[2] R. Santo,[3] H. R. Schmidt,[1] T. Siemiarczuk,[1],‡ S. P. Sorensen,[2,6] E. Stenlund,[4] M. L. Tincknell,[2],§ and G. R. Young[2]
WA80 Collaboration
[1] *Gesellschaft für Schwerionenforschung, Darmstadt, Federal Republic of Germany*
[2] *Oak Ridge National Laboratory, Oak Ridge, Tennessee 37831*
[3] *University of Münster, Münster, Federal Republic of Germany*
[4] *University of Lund, Lund, Sweden*
[5] *Lawrence Berkeley Laboratory, Berkeley, California 94720*
[6] *University of Tennessee, Knoxville, Tennessee 37996*
(Received 18 June 1991)

Distributions of transverse energy, forward energy, and $dE_T/d\eta$ from 60A and 200A GeV ^{16}O-induced and 200A GeV ^{32}S-induced nuclear collision with C, Al, Cu, Ag, and Au are presented. The energy, projectile, target, and centrality dependences are shown and discussed within a simple Glauber spectator-participant model. Two universal parametrizations of the $dE_T/d\eta$ distributions are presented together with various estimates of the nuclear stopping power and attained energy densities. An upper limit for $\gamma_{\text{direct}}/\pi^0$ in central collisions of 200A GeV ^{32}S + ^{197}Au is derived.

I. INTRODUCTION

The aim of the high-energy heavy-ion programs at the CERN Super Proton Synchrotron and Brookhaven Alternating Gradient Synchrotron accelerators is to study nuclear matter under conditions of extremely high densities and temperatures [1]. Theoretical calculations [1] predict that under such conditions hadronic matter might undergo a phase transition to a new form of matter, the quark-gluon plasma (QGP), in which quarks and gluons are deconfined over an extended volume. A broad spectrum of possible plasma signatures has been suggested [1]. An unfortunate common characteristic of most of these signatures is the necessity to distinguish them from the background created by ordinary hadronic processes. A thorough understanding of the reaction mechanisms in high-energy heavy-ion collisions is, therefore, an important prerequisite in any QGP search. Global event quantities like the transverse energy E_T, the forward energy E_F, and the transverse energy pseudorapidity density $dE_T/d\eta$ have proven to be valuable tools for obtaining this understanding of the reaction mechanisms [2–9].

It is the purpose of this paper to present results concerning the global parameters extracted from WA80's calorimeters in a series of measurements using beams of ^{16}O and ^{32}S bombarding nuclear targets. Section II contains a brief description of the experimental setup followed in Section III by a detailed discussion of the off-line method for extracting information on the transverse energy and $dE_T/d\eta$. In Section IV the minimum bias cross sections are presented together with a discussion of the total reaction cross sections calculated in the Glauber model. The systematic dependencies of the forward energy, transverse energy, and $dE_T/d\eta$ distributions on projectile and target mass, bombarding energy, and reaction centrality are presented in the Sections V–VIII, respectively. The emphasis in this article is to present the data together with a minimum of model assumptions. We have therefore chosen to discuss the data in terms of a simple spectator-participant model based on Glauber theory, which is discussed in Section VII, and avoid any specific comparisons to high-energy nuclear collision Monte Carlo models in the present paper. The use of the Glauber model is in line with the emphasis WA80 has put on the concept of participants [4] for obtaining a simple understanding of the transverse energy production. The model is utilized in Section IX to obtain two universal parametrizations of the $dE_T/d\eta$ distributions. In Section X several different estimates of the nuclear stopping power are presented together with a discussion of the relative merits of these estimates. Finally, Section XI presents simple estimates of the attained energy densities based on Bjorken's approach.

II. EXPERIMENTAL SETUP

The experiments were performed with the WA80 experimental setup [10] in the H3 beam line at the CERN Super Proton Synchroton (SPS). Beams of 60A GeV and 200A GeV ^{16}O bombarded targets of C, Cu, Ag, and Au and a beam of 200A GeV ^{32}S bombarded targets of Al, Cu, Ag, and Au. The beam intensity was typically up to 5×10^5 ions per second during beam spills.

The data presented here were obtained with a subset of the WA80 detectors consisting of two calorimeters: the midrapidity calorimeter (MIRAC) and the zero-degree calorimeter (ZDC). The construction, calibration, performance, and monitoring of these detectors has been described previously [11, 12]. MIRAC consists of 30 stacks with each stack subdivided into six 20 × 20 cm^2 towers. Each tower consists of a lead/scintillator electromagnetic section of 15.6 radiation lengths (0.8 absorption length) and an iron/scintillator hadronic section of 6.1 absorption lengths. The ZDC is a 60 × 60 cm^2 uranium/scintillator calorimeter divided into an electromagnetic section of 20.5 radiation lengths and a hadronic section of 9.6 absorption lengths. The geometrical configuration of the calorimeters in the ^{32}S experiment was identical to that used in the ^{16}O experiment [4]. MIRAC had full azimuthal coverage in the pseudorapidity interval $2.4 < \eta < 5.5$. For $1.6 < \eta < 2.4$ the azimuthal coverage of MIRAC varied from 10% up to 100%. The ZDC measured the integrated event energy for particles going through a 7.5 × 7.5 cm^2 hole in MIRAC. The effective distance of the hole from the target was 750 cm giving the ZDC a coverage in pseudorapidity of $\eta > 6.0$. In the interval $5.5 < \eta < 6.0$ MIRAC had only partial coverage and this interval was excluded from the analysis.

The minimum bias trigger condition was defined by the following two requirements: (a) less than 88% of the full beam energy recorded by the ZDC and (b) at least one charged particle recorded by the multiplicity arrays in the interval $1.3 < \eta < 4.4$. Table I shows target thicknesses and the number of events utilized in the analysis for the various targets.

III. CALCULATION OF E_T AND $dE_T/d\eta$

The procedures for the analysis of the MIRAC and ZDC data are documented in [11, 12]. Only the calculation of the transverse energy was changed significantly from the method described therein. The details of the WA80 E_T algorithm are discussed below.

TABLE I. Target thicknesses and the total number of analyzed events for all investigated projectile-target combinations.

Target	Thickness (interaction length)	No. of analyzed events 60A GeV ^{16}O	200A GeV ^{16}O	200A GeV ^{32}S
C	0.23%	243000	286000	
Al	0.19%			276000
Cu	0.15%	280000	259000	59000
Ag	0.13%	137000	228000	60000
Au	0.13%	337000	278000	318000

Theoretically E_T is defined as the sum of the transverse masses m_T of all $\mathcal{M}$ interacting and produced particles

$$E_T = \sum_{i=1}^{\mathcal{M}} (m_T)_i \ , \qquad m_T = \sqrt{p_T^2 + m^2} \ , \quad c \equiv 1 \ . \tag{1}$$

Experimentally $\hat{E}_T$ is, however, usually defined as

$$\hat{E}_T = \sum_{i=1}^{\mathcal{M}} \sin\theta_i \, E_i \ , \tag{2}$$

where θ_i and E_i are the scattering angle and total energy, respectively. At ultrarelativistic energies the two definitions are practically identical. In calorimeter-based experiments E_T is calculated conventionally as a calibrated sum over signals seen in all detector elements

$$E_T = \sum_{n=1}^{N_d} \tilde{C}_n S_n \ , \tag{3}$$

where N_d is the number of detector elements (channels) of the calorimeter, S_n is the calibrated signal recorded in the nth channel, and $\tilde{C}_n$ is a set of coefficients adjusted from simulations so that $< E_T >_e = < \hat{E}_T >_e$, where the average $< x >_e$ is performed over a large set of simulated events corresponding to the particular event type of interest. The tilde indicates a quantity obtained from simulations. $\tilde{C}_n$ will usually be close to $\sin\theta_n$, where θ_n is the polar angle of the nth detector element, but more refined approaches will include realistic event topologies and the detector response in the calculation of $\tilde{C}_n$ [11]. The set of $\tilde{C}_n$'s might futhermore be dependent on additional parameters like $\sum S_n$, charged particle multiplicity, etc.

This empirical approach to the evaluation of E_T has been generalized by WA80 to the calculation of $dE_T/d\eta$. Let α be an index running over a suitable set of pseudorapidity η bins for hadronic and electromagnetic particles separately. In analogy with (3) $dE_T/d\eta$ for a particular value of α can be calculated on an event-by-event basis as

$$(dE_T/d\eta)_\alpha = \sum_{n=1}^{N_d} \tilde{D}_{\alpha n} S_n \ , \tag{4}$$

where

$$\tilde{D}_{\alpha n} = \frac{< \sin\theta_\alpha >_e}{< \tilde{A}_\alpha >_e \, \Delta_\alpha} \frac{< \sum_{j=1}^{\mathcal{M}_\alpha} \tilde{E}_{jn} >_e}{< \tilde{S}_n >_e} \ . \tag{5}$$

$\tilde{\mathbf{D}}$ is called the η-distribution matrix and is equivalent to the $\tilde{C}$ coefficient vector in (3). θ_α, Δ_α, and $\tilde{A}_\alpha$ are the scattering angle, the η width, and the acceptance of the detector in the η interval α, respectively. $\mathcal{M}_\alpha$ is the

multiplicity of particles in the η interval α and $\tilde{E}_{jn}$ is the part of the energy of particle j which is deposited in detector element n. Finally, S_n is the total calibrated signal recorded in element n. Note that the energy deposited E_n and the calibrated signal S_n recorded in a particular element n differ due to different e/h ratios and calibrations of the electromagnetic and hadronic sections [11].

The simulations were based on minimum bias events obtained from the event generators FRITIOF V1.07 [13], VENUS V3.05 [14], and HIJET [15] combined with the measured response function of MIRAC [11]. This procedure corrects for effects originating from detector response and nonprojective geometry and enables a separation of the amount of electromagnetic (i.e., photons and electrons) and hadronic energy. $\tilde{\mathbf{D}}$ will in principle depend on the assumed event topology. It was found, however, that for a fixed value of the bombarding energy $\tilde{\mathbf{D}}$ varied only slightly for different projectile-target combinations, impact parameters, and choices of event generator and a single $\tilde{\mathbf{D}}$ matrix could be used, since the differences among the resulting $dE_T/d\eta$ distributions were smaller than the experimental errors on the distributions.

E_T for a particular interval of η was obtained by integrating $dE_T/d\eta$. This integration could be performed on an event-by-event basis within the interval $2.4 < \eta < 5.5$. $dE_T/d\eta$ could, however, be obtained averaged over a particular event class for the full MIRAC η coverage of $1.6 < \eta < 5.5$. For the ^{16}O data the maximum deviation between the results obtained with the $\tilde{\mathbf{D}}$-matrix method and the previously published data [4] was less than 5%. All results in this publication have been obtained using the $\tilde{\mathbf{D}}$-matrix method [16]. The estimated systematic error in the overall transverse energy scale for the interval $2.4 < \eta < 5.5$ is less than 10% and for the more limited interval $2.4 < \eta < 3.5$ the systematic error is less than 5%.

IV. REACTION CROSS SECTIONS

The absolute minimum bias cross sections, as shown in Table II, are calculated from the number of beam and minimum bias triggers and the target thicknesses. All cross sections and spectra in this paper have been corrected for background effects by subtracting the normalized results from runs on an empty-target aluminium frame. The background corrections to the uncorrected minimum bias cross sections are typically between 5% and 20% and only affect the E_F and E_T spectra for extremely peripheral events. The systematic error on the absolute cross section scale is estimated to be less than 10%.

TABLE II. Experimental minimum bias cross sections and calculated total reaction cross sections based on Glauber theory. The parameters r_0 and r_b are Bradt-Peters parameters defined in Eq. (10)

Target	Minimum bias σ (mb)			Glauber σ (mb)	
	60A GeV	200A GeV			
	^{16}O	^{16}O	^{32}S	^{16}O	^{32}S
C	650	450		1110	1480
Al			1200	1510	1930
Cu	1650	1350	1620	2150	2650
Ag	2250	1800	2190	2680	3230
Au	2900	2450	2970	3490	4120
r_0 (fm)	1.46	1.44	1.38	1.31	
r_b (fm)	2.35	3.01	2.53	0.28	

The minimum bias trigger conditions described in Section II exclude the most peripheral collisions. In order to obtain an estimate of this distortion the total reaction cross sections $\sigma_{\rm tot}$ have been calculated based on Glauber theory [17–20]:

$$\sigma_{\rm tot} = \int d\mathbf{b}\, \mathcal{C}(\mathbf{b}) ,$$

$$\mathcal{C}(\mathbf{b}) = 1 - [1 - \sigma_{nn}\mathcal{T}(\mathbf{b})]^{A_t A_p} , \tag{6}$$

$$\mathcal{T}(\mathbf{b}) = \int d\mathbf{s}_t\, T_t(\mathbf{s}_t) T_p(\mathbf{b} - \mathbf{s}_t) .$$

$\mathcal{C}(\mathbf{b})$ is the reaction probability at the impact parameter $\mathbf{b}$ and expresses the probability that at least one nucleon from the target hits at least one nucleon from the projectile. The number of nucleons in the projectile and target are A_p and A_t, respectively, and $\sigma_{nn} = 32$ mb is the free nucleon-nucleon inelastic cross section. $\mathcal{T}(\mathbf{b})$ is the nucleus-nucleus thickness function and $T(\mathbf{s})$ is the individual nucleus thickness function defined as

$$T(\mathbf{s}) = \int dz\, \rho(r) ,$$

$$\mathbf{r} = \mathbf{s} + \mathbf{z} , \tag{7}$$

where ρ is the nuclear density distribution, z is the longitudinal coordinate, and $s = \sqrt{x^2 + y^2}$ is the transverse coordinate. For nuclei with $A \geq 12$ the spherical Woods-Saxon density distribution has been used

$$\rho(r) = \mathcal{N}_\rho \left(1 + \exp\left[\frac{r - R}{a}\right]\right)^{-1} ,$$

$$R = 1.16A^{1/3} - 1.35A^{-1/3} \text{ fm} , \tag{8}$$

$$a = 0.54 \text{ fm}$$

with numerical parameters calculated from a χ^2 fit to nuclear charge density data from electron scattering [21]. $\mathcal{N}_\rho$ is determined from the normalization condition

$$\int d^3r\, \rho(r) = 1 . \tag{9}$$

The energy-independent $\sigma_{\rm tot}$'s calculated from (6) are shown in Table II. $\sigma_{\rm tot}$ is considerably larger than the experimentally measured minimum bias cross section $\sigma_{\rm mb}$. At 200A GeV $\sigma_{\rm mb}/\sigma_{\rm tot}$ varies from 0.40 to 0.72 for increasing target mass whereas at 60A GeV this ratio is larger and varies from 0.59 to 0.83. The reasons for these

variations will be explained in Section V.

The projectile-target dependence of the cross sections can be parameterized by the sum of the transverse areas of the nuclei as expressed in the Bradt-Peters expression [22–24]

$$\sigma = \pi(r_0 A_p^{1/3} + r_0 A_t^{1/3} - r_b)^2 \ . \tag{10}$$

The radius parameter r_0 and the overlap parameter r_b are shown in Table II. The overlap parameter is close to zero for the total Glauber reaction cross sections whereas the minimum bias cross sections show a large value of r_b. This indicates that r_b to a larger extent is a measure of the amount of trigger bias in an experiment rather than an estimate of the amount of overlap between the two nuclei necessary for an inelastic reaction to take place.

V. FORWARD ENERGY

The energy deposited in the zero-degree calorimeter is called the forward energy, E_F, by WA80 and corresponds to the sum of the energy of all particles with scattering angles smaller than $\approx 0.3°$ ($\eta > 6$). The E_F spectra for both ^{16}O- and ^{32}S-induced reactions shown in Fig. 1 can be qualitatively understood based on the following simple arguments. For peripheral collisions E_F will be dominated by the energy carried by projectile spectators resulting in large values of E_F. Since the differential cross section is increasing with impact parameter, the E_F spectra will be increasing for large E_F until the trigger cut sets in at $\approx$ 88% of the beam energy. For central collisions, where most or all of the projectile nucleons participate, only the energy carried by the most forward-going leading particles and reaction products will reach the ZDC resulting in small values of E_F. The range of impact parameters b over which the entire projectile will react with the target is approximately given by $b < R_t - R_p$, where R_p and R_t are the radii of the projectile and target, respectively. The ratio of central events to the total number of events in asymmetric collisions ($A_p < A_t$) can therefore be expressed in the "sharp sphere" approximation as

$$\frac{\sigma_{\text{central}}}{\sigma_{\text{tot}}} \approx \frac{\pi(R_t - R_p)^2}{\pi(R_t + R_p)^2} = \left(\frac{A_t^{1/3} - A_p^{1/3}}{A_t^{1/3} + A_p^{1/3}}\right)^2 \ . \tag{11}$$

The "bump" observed at $\approx 0.1 E_{\text{beam}}$ in the E_F spectra for the heaviest targets corresponds to these central events and (11) demonstrates that the size of the bump will increase with increasing target mass for a fixed projectile and decrease with increasing projectile mass as observed in Fig. 1.

The importance of the nuclear geometry in the determination of the shape of energy spectra in high-energy nuclear collisions can be illustrated by the following scaling law. The shape of the E_F spectra at 200A GeV scales approximately with the geometric ratio R_t/R_p or stated more precisely

$$\frac{d\sigma}{de} \approx \sigma_{\text{tot}} f\left(e, \frac{R_t}{R_p}\right) \ ,$$

$$e = E_F / E_{\text{beam}} \ . \tag{12}$$

$$\sigma_{\text{tot}} = \pi r_0^2 (A_t^{1/3} + A_p^{1/3})^2 \ .$$

Examples of this scaling law are the similarities between the E_F spectra for O + Ag and S + Au, where the ratios between the radii are 1.89 and 1.83, respectively, and the spectra for O + C and S + Al with ratios of 0.91 and 0.94, respectively.

Based on the above discussion of the E_F spectra we are now in a position to understand the variation of σ_{mb}

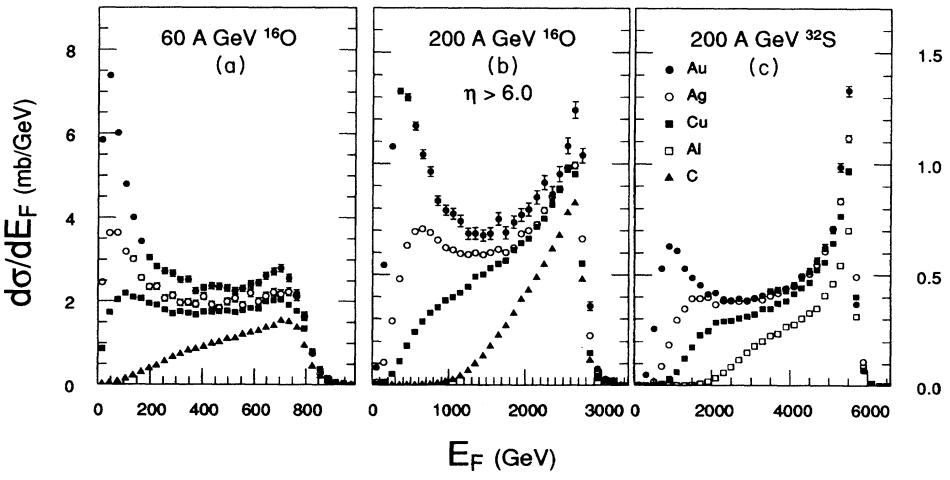

FIG. 1. Forward energy spectra for heavy ion reactions induced by (a) 60A GeV ^{16}O, (b) 200A GeV ^{16}O, and (c) 200A GeV ^{32}S. The error bars reflect the statistical errors. At energies below 700, 2600, and 5500 GeV for (a), (b), and (c), respectively, the spectra are corrected for distortions caused by trigger cuts and background events. The vertical scales in (b) and (c) are identical.

in Table II: For a given impact parameter the most stringent trigger condition (a) can be expressed as

$$\frac{E_F}{E_{\rm beam}} = \frac{E_{S_p}}{E_{\rm beam}} + \frac{E_R[\eta > 6]}{E_{\rm beam}} \leq 0.88 \qquad (13)$$

where E_{S_p} is the energy carried by the projectile spectators and E_R and $E_R[\eta > 6]$ are the energies carried by all the reaction products and the reaction products with $\eta > 6$, respectively. When $E_{\rm beam}$ is increased from 60A GeV to 200A GeV the nucleon-nucleon CM rapidity increases from 2.4 to 3.0 and as a consequence the ratio $E_R[\eta > 6]/E_{\rm beam}$ will increase. In order to fulfill the trigger condition (13) the ratio $E_{S_p}/E_{\rm beam}$ must decrease which implies larger nuclear overlap and smaller impact parameters and thereby smaller minimum bias cross sections.

The increase of $\sigma_{\rm mb}/\sigma_{\rm Glauber}$ with increasing target mass follows from the shape of the E_F spectra. For the lighter targets a large fraction of the E_F is above 88% of $E_{\rm beam}$, whereas for the heavier targets this fraction is smaller, resulting in reduced trigger bias.

VI. TRANSVERSE ENERGY

The ^{16}O- and ^{32}S-induced E_T spectra, as shown in Fig. 2, share a set of features which, apart from trigger bias, can also be understood primarily from the nuclear overlap geometry. At very low energies ($E_T < 0.1E_T^{\rm max}$) the spectra fall off due to the trigger bias against the most peripheral events. Spectra with less peripheral bias, as measured by NA34 [5] and NA35 [2], show a dramatic increase at low E_T. Above $\approx 0.2\ E_T^{\rm max}$ the spectra decrease either slowly or are approximately constant. For the heaviest targets this plateau ends in a bump which is followed by a rapidly falling tail of Gaussian shape [25]. As discussed in [4] E_T and E_F display a narrow anticorrelation. This leads to an interpretation of the E_T spectra in terms of decreasing impact parameter for increasing E_T. The long plateau corresponds to reactions in which successively more of the projectile overlaps the target, and the bump can be identified with central collisions in which the entire projectile is engulfed by the target as discussed in Section V. The Gaussian tail at large E_T values is observed to extend over more than 5 decades. An earlier analysis [25] suggests that this tail is largely due to fluctuations in the number of participating nucleons rather than to variations in the E_T produced per emitting source.

A comparison between the ^{16}O- and ^{32}S-induced E_T spectra at 200A GeV shows that in the tail region the ratio between E_T for S+Au and O+Au is ≈ 1.65. This value is, however, strongly dependent on the particular η interval over which E_T is integrated. For the interval $-0.1 < \eta < 2.9$ NA34 [6] finds a ratio of ≈ 1.50. In Section VIII it will be demonstrated how these different ratios are a simple consequence of the decreasing dependence on projectile mass at decreasing η values.

For 200A GeV the maximum E_T for $2.4 < \eta < 5.5$ is observed to increase with increasing target mass, whereas $E_T^{\rm max}$ is approximately constant at 60A GeV. A target-independent maximum E_T at 15A GeV for $1.25 < \eta < 2.44$ has been interpreted by E802 [3] as an indication for full stopping. For target rapidities $-0.5 < \eta < 0.8$ at 15A GeV E814 [7], however, finds a strong increase in E_T as a function of target mass. This indicates that a target-independent $E_T^{\rm max}$ measured over a limited η interval is not a sufficient condition for establishing full nuclear stopping. This conclusion can be further substantiated at 60A GeV. Our measurement of a target-independent $E_T^{\rm max}$ at forward rapidities, which could be prematurely interpreted as evidence for full nuclear stopping, can be supplemented at this energy by the additional observation from NA34 [5] that for $-0.1 < \eta < 2.9$ $E_T^{\rm max}$ shows a strong target dependence, which by NA34 [5, 27] is interpreted as inconsistent with

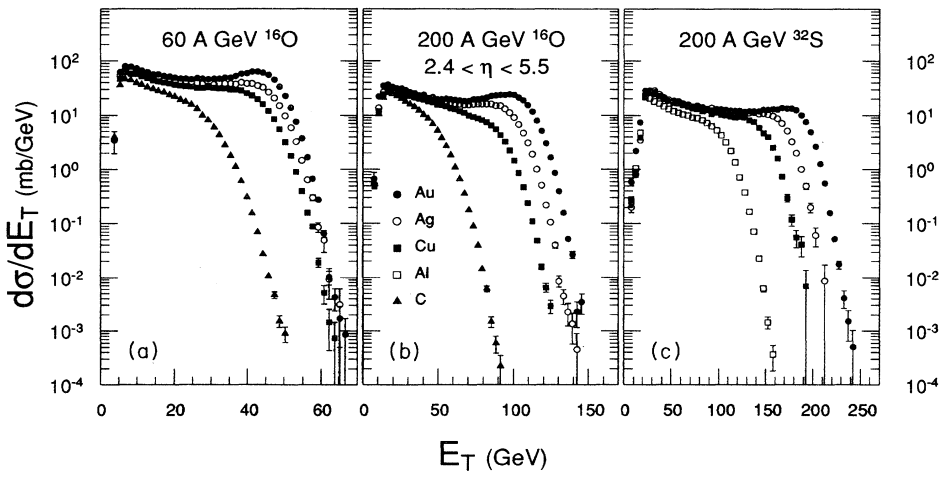

FIG. 2. Transverse energy spectra for heavy ion reactions induced by (a) 60A GeV ^{16}O, (b) 200A GeV ^{16}O, and (c) 200A GeV ^{32}S. The error bars reflect the statistical errors. At energies above 8 GeV, 20 GeV, and 30 GeV for (a), (b), and (c), respectively, the spectra are corrected for distortions caused by background events.

full nuclear stopping. Within the Landau hydrodynamical model it is possible to obtain scenarios with full stopping and target-dependent E_t distributions, but recent calculations based on this model by Stachel and Braun-Munzinger[26] indicate that full stopping is not reached at 60A GeV.

The $\tilde{\mathbf{D}}$-matrix method described in Section III makes it possible to separate the observed E_T into electromagnetic $E_{T,\mathrm{em}}$ and hadronic $E_{T,\mathrm{had}}$ components based on the signals recorded in the electromagnetic (S_{em}) and hadronic (S_{had}) longitudinal sections of MIRAC. An example of the resulting distributions of $E_{T,\mathrm{em}}$ and $E_{T,\mathrm{had}}$ is shown in Fig. 3. The $\tilde{\mathbf{D}}$-matrix method performs this separation well as long as the ratio $S_{\mathrm{em}}/S_{\mathrm{had}}$ does not deviate greatly from the ratios calculated by the event generators (VENUS, FRITIOF, and HIJET) on which the $\tilde{\mathbf{D}}$ matrix is based. If, however, an event contained purely electromagnetic energy then the $\tilde{\mathbf{D}}$-matrix algorithm would incorrectly assign approximately 1/3 of the EM signal as hadronic energy. Simulations show that central events with an artificial increase or decrease of a factor of two in electromagnetic energy will be assigned values of $E_{T,\mathrm{em}}$ by the $\tilde{\mathbf{D}}$ matrix which deviate less than 10% from the correct value. The accuracy of the method increases rapidly with multiplicity or E_T, since shower deposition fluctuations decrease with increasing event multiplicity. Investigations of more than 2×10^6 events of S_{em} vs S_{had} revealed no exotic events with ratios $S_{\mathrm{em}}/S_{\mathrm{had}}$ deviating dramatically from the values predicted by the event generators, such as "Centauro" events [29] with abnormal low electromagnetic energy content. A similar conclusion can be drawn from Fig. 4, which shows a contour plot of the ratio E_T^{em}/E_T vs E_T. Note the symmetry of the distribution along the ordinate and the absence of any group of events with abnormal electromagnetic content.

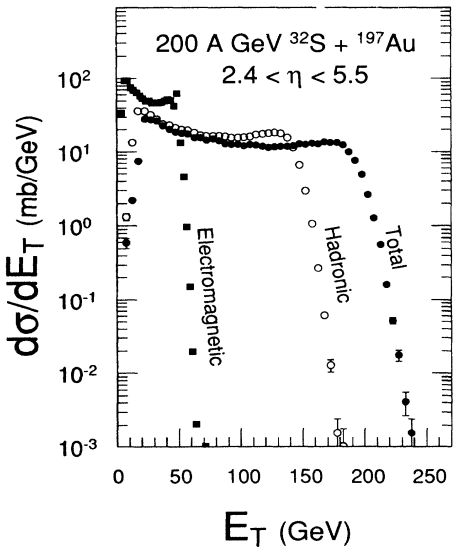

FIG. 3. Electromagnetic, hadronic, and total transverse energy for 200A GeV ^{32}S + ^{197}Au. The electromagnetic and hadronic contributions have been separated with the $\tilde{\mathbf{D}}$-matrix method described in Section III.

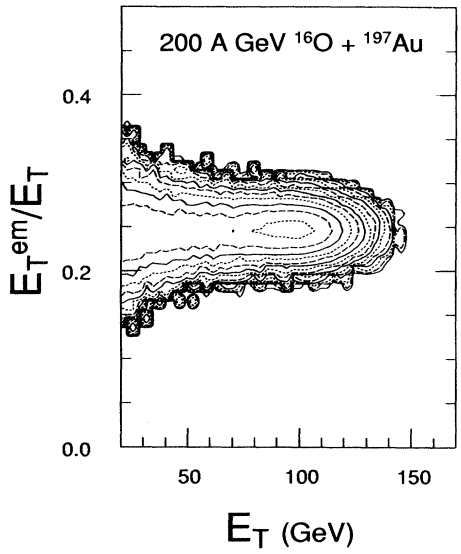

FIG. 4. Contour plot of E_T^{em}/E_T vs E_T for $2.4 < \eta < 5.5$. The outermost contour is set just below the 1 count/channel level and each successive contour corresponds to an increase of the yield/channel by a factor of 2. The spectrum has not been smoothed.

One motivation for extraction of the electromagnetic energy of the event is the expectation that an increased number of direct photons should be produced in central collisions if a quark-gluon plasma is formed. These photons would lead to an increased fraction of electromagnetic energy as suggested, e.g., in [30]. The results of such a search for an enhanced electromagnetic component are shown in Fig. 5, which have been obtained from plots similar to Fig. 4 by linear regression along the ordinate. Please note that the abscissas in Figs. 4 and 5 are E_T and E_F, respectively. The ratio $< E_T^{\mathrm{em}}/E_T >$ is observed to have a value of ≈ 0.25 and to be constant at 200A GeV over a large range of E_F and for two widely different systems like ^{16}O + ^{12}C and ^{32}S + ^{197}Au. At 60A GeV, where the probability for QGP formation is considered less likely, the ratio $< E_T^{\mathrm{em}}/E_T >$ is, however, seen to decrease with increasing E_F. The most likely reason for this behaviour at 60A GeV is an increased hadronic energy content at $\eta < 5.5$ for peripheral events caused by projectile fragmentation. This enhanced probability for observing projectile spectator fragments in MIRAC at 60A GeV as compared to 200A GeV was discussed in [4] as an explanation for the observation that at 60A GeV the E_F was considerably less than predicted by Monte Carlo simulation codes with no projectile break-up included.

The observation that at 200A GeV the ratio $\langle E_T^{\mathrm{em}}/E_T \rangle$ is approximately independent of centrality can be used to estimate an upper limit for the direct photon production at 200A GeV. If it is assumed that (a) all ^{16}O + ^{12}C collisions and peripheral ^{32}S + ^{197}Au collisions have no direct photon component, (b) all electromagnetic energy

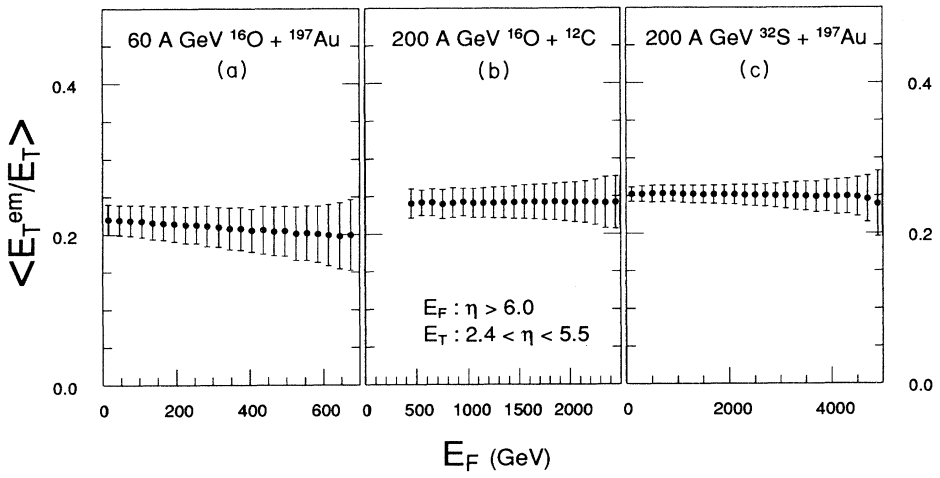

FIG. 5. Ratio of electromagnetic E_T to total E_T as a function of E_F for (a) 60A GeV ^{16}O + ^{197}Au, (b) 200A GeV ^{16}O + ^{12}C, and (c) 200A GeV ^{32}S + ^{197}Au. The solid points show the average ratio calculated by linear regression along the ordinate. The bars reflect the standard deviation of the distributions along the ordinate.

in these collisions originates from π^0 decay photons, and (c) the average energy of the direct photons and the decay photons is the same, and if it is conservatively estimated that the maximal increase of $< E_T^{\rm em}/E_T >$ between peripheral and central events is less than 10% (see Fig. 5) then an estimate of the upper limit for the p_T integrated γ/π^0 in central ^{32}S + ^{197}Au collisions is 20%. If it is, however, assumed that the direct photons and the π^0's have the same average energy then this upper limit is reduced to 10%. These estimates are consistent with the upper limit of 15% obtained with much fewer assumptions from the WA80 photon detector SAPHIR [31] for proton- and ^{16}O-induced reactions at 60A GeV and 200A GeV.

VII. IMPACT PARAMETER SELECTION

In any analysis of data obtained for different projectile-target combinations it is important to be able to perform comparisons for similar event classes such as central events or peripheral events. This requires a method for estimating the impact parameter on an event-by-event basis. For this purpose the following procedure has been developed.

The basic assumption is that E_F depends monotonically on b. From this it follows that the impact parameter b' corresponding to a particular value of the forward energy E_F' can be estimated from

$$\pi b'^{\,2} = \int_0^{E_F'} \frac{d\sigma}{dE_F} dE_F \tag{14}$$

where $d\sigma/dE_F$ is the E_F spectrum. Computer simulations based on FRITIOF and VENUS indicate that this method allows b to be estimated to within ± 1 fm except for the most central events in asymmetric systems, where the monotonic correlation between b and E_F is washed out for $b < R_t - R_p - 1$ fm.

This method for estimating the impact parameter on an event-by-event basis enables us to employ the following definitions for three important event classes:

$$\begin{aligned} &\text{central} \equiv b < R_t - R_p \ , \\ &\text{intermediate} \equiv R_t - R_p < b < R_t \ , \\ &\text{peripheral} \equiv R_t < b < R_{mb} \ , \\ &\qquad R = 1.2A^{1/3} \ \text{fm} \ , \end{aligned} \tag{15}$$

where $R_{\rm mb} = \sqrt{\sigma_{\rm mb}/\pi}$. Clearly for certain projectile-target combinations a particular event class, according to the above classification scheme, will not exist, like, e.g., central collisions for ^{16}O + ^{12}C. In an earlier paper [4] WA80 has shown that the E_T generated in a heavy-ion collision is approximately proportional to the total number of participant nucleons. In Sections VIII–X the concept of participants will again be used extensively in order to gain a better understanding of the data. In contrast to Ref. [4], where the number of participants were found from FRITIOF calculations, we will here employ a simpler and more transparent method for extracting this information from the data based on Glauber theory [17, 20].

Following the notation for Glauber theory introduced in Eqs. (6)–(9) in Section IV the probability $\mathcal{P}(W_t, b)$ for a particular value of the number of target participants W_t at a particular impact parameter b will be given by a binomial distribution

$$\begin{aligned} &\mathcal{P}(W_t, b) = C_{W_t}^{A_t} [P_{tp}(b)]^{W_t} [1 - P_{tp}(b)]^{A_t - W_t} \ , \\ &P_{tp}(b) = \int d\mathbf{s}_t \ T_t(\mathbf{s}_t) \{1 - [1 - \sigma_{nn} T_p(\mathbf{s}_t - \mathbf{b})]^{A_p}\} \ , \\ &C_{W_t}^{A_t} = \frac{A_t!}{W_t!(A_t - W_t)!} \ . \end{aligned} \tag{16}$$

$P_{tp}(b)$ is the probability that a target nucleon is struck by any projectile nucleon during a collision at impact parameter b.

The average number of target participants $\overline{W}_t(b)$ at a given impact parameter b will be given by

$$\overline{W}_t(b) = P_{tp}(b) A_t \ . \tag{17}$$

Since all data in this paper have been impact-parameter selected using E_F distributions with Eqs. (14) and (15), it is necessary to find the number of target participants $\overline{W}_t$ averaged over a particular interval of impact parameters $[b_{\min}, b_{\max}]$. This has been done according to the following equation:

$$\overline{W}_t = \frac{2\ A_t}{b_{\max}^2 - b_{\min}^2} \int_{b_{\min}}^{b_{\max}} db\ b P_{tp}(b) \ . \tag{18}$$

The probability of encountering a particular value of projectile participants $\mathcal{P}(W_p, b)$ and the average number of projectile participants $\overline{W}_p$ can be calculated from (16)–(18) by exchanging the projectile and target indices p and t. Finally, the total number of participants is simply the sum of the projectile and target participants

$$W = W_p + W_t \ , \tag{19}$$

$$\overline{W} = \overline{W}_p + \overline{W}_t \ . \tag{20}$$

The method outlined above for extracting the collision impact parameter and the number of participants will be used extensively in the rest of the paper in discussions of the experimental results.

VIII. $dE_T/d\eta$ DISTRIBUTIONS

In this section the dependence of the $dE_T/d\eta$ distributions on impact parameter, target, projectile, and beam energy will be discussed. All of the $dE_T/d\eta$ distributions presented for a particular event class have been fitted with Gaussian functions. These fits are also presented as curves through the data points in Figs. 6–10. The three free parameters in these fits (1) the height of the distribution $dE_T/d\eta|_{\max}$, (2) the centroid $\overline{\eta}$, and (3) the standard deviation σ_η are presented in Tables III–V, respectively. The use of a Gaussian fit in order to calculate $\overline{\eta}$ and σ_η was necessary since WA80 does not have full η coverage. The χ^2 per degree of freedom for the fits were typically ranging from 0.3 to 0.5. Since additional free parameters did not decrease the χ^2, it was concluded that the characterization of each $dE_T/d\eta$ distribution by a Gaussian shape with three free parameters exhausts the full information content in the measured distributions.

The dependence of the $dE_T/d\eta$ spectra on the impact parameter of the collision is shown in Fig. 6. The three distributions correspond to central, intermediate, and peripheral collisions as defined in (15). A more complete picture of the impact parameter dependence can be obtained by comparing the same three event classes in Tables III–V. For the system 200A GeV ^{32}S + ^{197}Au shown in Fig. 6 the following impact parameter dependence is observed: (a) $dE_T/d\eta|_{\max}$ increases from 15 GeV for peripheral collisions to 93 GeV in central collisions, (b) the centroid decreases from $\eta = 3.0$ to $\eta = 2.6$, and (c) the standard deviation decreases from $\sigma = 1.7$ to $\sigma = 1.4$.

TABLE III. $dE_T/d\eta|_{\max}$ determined from Gaussian fits to the $dE_T/d\eta$ distributions. The three event classes are defined in (15). The errors are dominated by the systematic uncertainty of 5% on the transverse energy scale for the outer region of MIRAC.

	$dE_T/d\eta\|_{\max}$ (GeV)		
Target	60A ^{16}O	200A ^{16}O	200A ^{32}S
	Central		
Cu	29.2 ± 1.5	42.2 ± 2.1	69.4 ± 3.5
Ag	33.4 ± 1.7	49.8 ± 2.5	81.9 ± 4.1
Au	39.5 ± 2.0	60.2 ± 3.0	92.9 ± 4.6
	Intermediate		
C	11.9 ± 0.6	16.2 ± 0.8	
Al			32.2 ± 1.6
Cu	19.7 ± 1.0	23.7 ± 1.2	47.1 ± 2.4
Ag	21.0 ± 1.1	30.0 ± 1.5	55.0 ± 2.7
Au	22.9 ± 1.1	33.6 ± 1.7	54.1 ± 2.7
	Peripheral		
C	5.7 ± 0.3	8.3 ± 0.4	
Al			13.7 ± 0.7
Cu	7.3 ± 0.4	9.6 ± 0.5	17.5 ± 0.9
Ag	7.3 ± 0.4	11.1 ± 0.6	18.8 ± 0.9
Au	7.4 ± 0.4	11.2 ± 0.6	15.3 ± 0.8

TABLE IV. η centroid of the $dE_T/d\eta$ distributions as determined from Gaussian fits.

	$\overline{\eta}$		
Target	60A ^{16}O	200A ^{16}O	200A ^{32}S
	Central		
Cu	2.34 ± 0.06	2.62 ± 0.06	2.89 ± 0.05
Ag	2.19 ± 0.07	2.44 ± 0.08	2.67 ± 0.07
Au	2.00 ± 0.08	2.19 ± 0.10	2.56 ± 0.06
	Intermediate		
C	2.81 ± 0.10	3.09 ± 0.05	
Al			3.23 ± 0.06
Cu	2.40 ± 0.05	2.73 ± 0.07	2.92 ± 0.06
Ag	2.30 ± 0.07	2.57 ± 0.08	2.78 ± 0.07
Au	2.16 ± 0.09	2.41 ± 0.10	2.73 ± 0.10
	Peripheral		
C	2.68 ± 0.07	2.97 ± 0.07	
Al			3.24 ± 0.07
Cu	2.51 ± 0.03	2.78 ± 0.10	3.01 ± 0.08
Ag	2.46 ± 0.09	2.71 ± 0.09	2.94 ± 0.08
Au	2.38 ± 0.10	2.67 ± 0.10	2.97 ± 0.10

TABLE V. Standard deviation in η of the $dE_T/d\eta$ distributions as determined from Gaussian fits.

	σ_η		
Target	$60A$ ^{16}O	$200A$ ^{16}O	$200A$ ^{32}S
	Central		
Cu	1.14 ± 0.06	1.43 ± 0.09	1.41 ± 0.10
Ag	1.15 ± 0.06	1.44 ± 0.10	1.44 ± 0.10
Au	1.16 ± 0.07	1.47 ± 0.10	1.39 ± 0.11
	Intermediate		
C	1.24 ± 0.15	1.47 ± 0.10	
Al			1.50 ± 0.10
Cu	1.23 ± 0.06	1.50 ± 0.11	1.48 ± 0.11
Ag	1.24 ± 0.07	1.50 ± 0.11	1.49 ± 0.11
Au	1.26 ± 0.07	1.55 ± 0.11	1.46 ± 0.15
	Peripheral		
C	1.34 ± 0.09	1.60 ± 0.13	
Al			1.64 ± 0.14
Cu	1.35 ± 0.06	1.63 ± 0.15	1.63 ± 0.14
Ag	1.37 ± 0.09	1.62 ± 0.13	1.65 ± 0.15
Au	1.39 ± 0.09	1.62 ± 0.13	1.69 ± 0.15

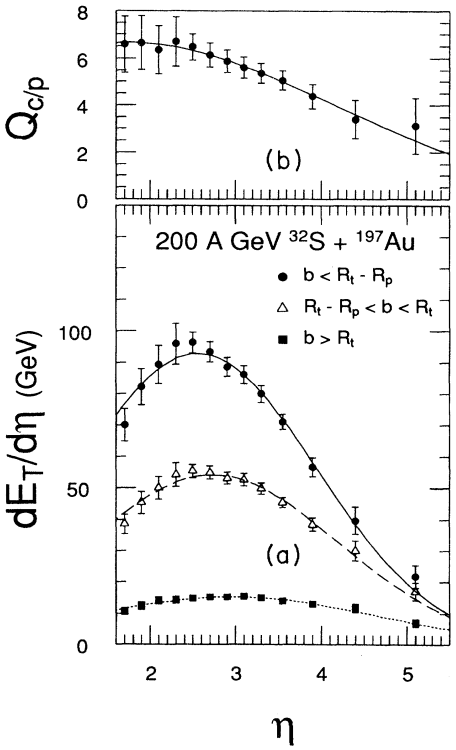

FIG. 6. (a) Dependence of $dE_T/d\eta$ for 200A GeV ^{32}S + ^{197}Au on impact parameter. The 3 distributions correspond from top to bottom to central, intermediate, and peripheral collisions as defined in Eqs. (15). The curves drawn through the data points in Figs. 6(a)–10(a) are Gaussian fits with parameters shown in Tables III–V. (b) Ratio $Q_{c/p}$ between the $dE_T/d\eta$ distribution for central and peripheral events.

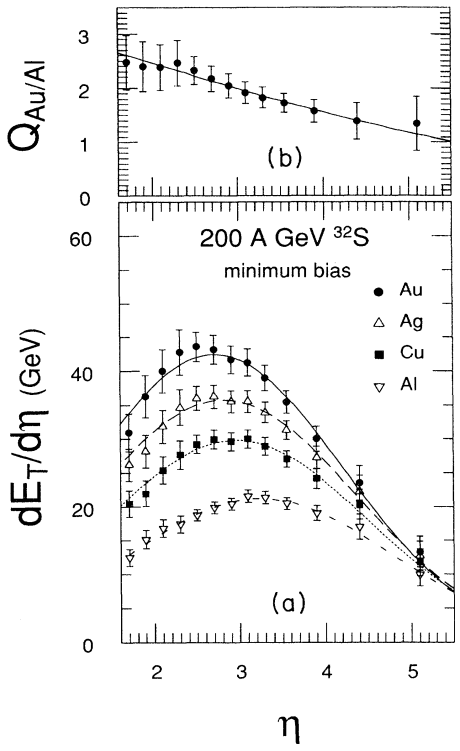

FIG. 7. (A) Target dependence of $dE_T/d\eta$ in 200A GeV ^{32}S-induced minimum bias collisions. (B) Ratio $Q_{\mathrm{Au/Al}}$ between $dE_T/d\eta$ distributions for ^{197}Au and ^{27}Al targets. See Fig. 6 for further details.

As seen in Fig. 6(b), $dE_T/d\eta$ increases much more rapidly at backward rapidities than at forward rapidities as a function of increasing centrality.

The dependence of $dE_T/d\eta$ on target mass is illustrated in Fig. 7. Qualitatively the effects of increasing the target mass are very similar to decreasing the impact parameter as can be seen by comparing Figs. 6 and 7. The η positions of the maxima of the distributions decrease from 3.2 for ^{27}Al to 2.7 for ^{197}Au.

A point of some controversy has been the projectile mass dependence of E_T in central collisions. As can be seen from Fig. 8 this dependence is strongly rapidity dependent. In the projectile rapidity region $dE_T/d\eta$ increases approximately proportional to the projectile mass A_p, whereas in the target rapidity region the dependence on A_p is much weaker. The scaling factor of 1.67 for E_T between ^{32}S- and ^{16}O-induced reactions quoted in Section VI corresponds to the average ratio between the two spectra in Fig. 8 in the interval $2.4 < \eta < 5.5$. The scaling factor of 1.50 measured by NA34 with a coverage of $-0.1 < \eta < 2.9$ also seems reasonable based on the decrease of the scale factor in Fig. 8(b) from 1.65 at $\eta = 3.0$ to 1.3 at $\eta = 1.6$

The dependence of $dE_T/d\eta$ on bombarding energy is illustrated in Fig. 9 for 60A GeV and 200A GeV ^{16}O + ^{197}Au collisions. The maximum value of $dE_T/d\eta$, the centroid, and the standard deviation are all seen to increase as functions of $\sqrt{s}$. The scaling factor shown in Fig. 9(b) is seen to increase dramatically at forward

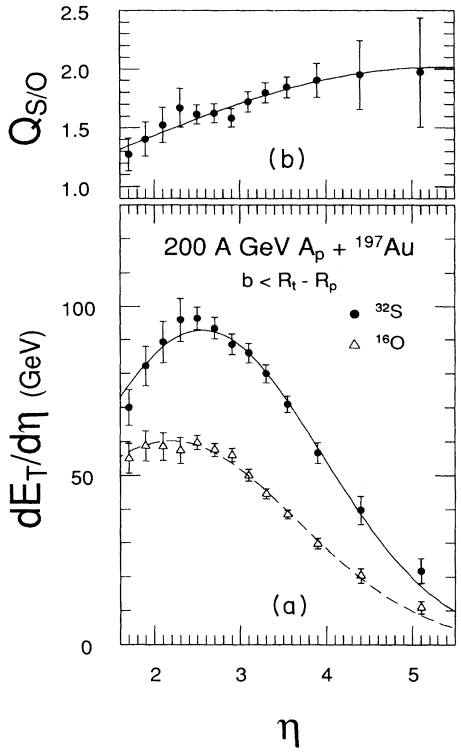

FIG. 8. (a) Projectile dependence of $dE_T/d\eta$ in 200A GeV A_p + ^{197}Au central collisions. (b) Ratio $Q_{S/O}$ between the $dE_T/d\eta$ distributions for ^{32}S- and ^{16}O-induced reactions. See Fig. 6 for further details.

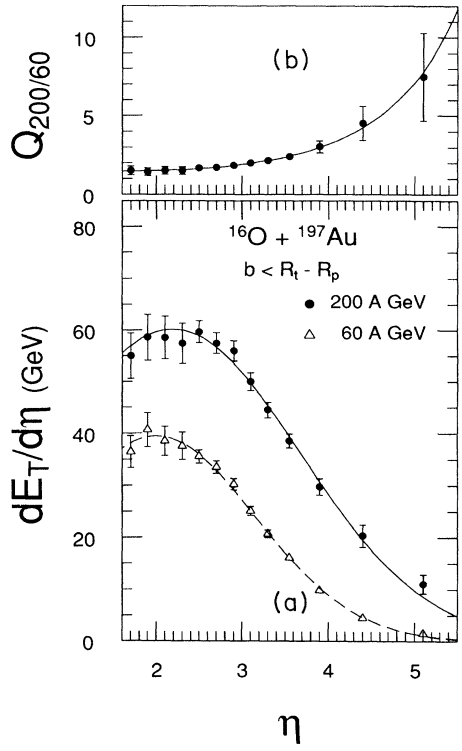

FIG. 9. (a) $dE_T/d\eta$ distributions for 60A GeV and 200A GeV ^{16}O + ^{197}Au central collisions. (b) Ratio $Q_{200/60}$ between $dE_T/d\eta$ distributions for 200A GeV and 60A GeV. See Fig. 6 for further details.

pseudorapidities. Note, that although the distribution is wider at 200A GeV than at 60A GeV, there is no evidence for a midrapidity plateau as assumed in the Bjorken model [32]. This is not surprising in view of (a) the narrowness of such a plateau even at ISR energies of $\sqrt{s}$ = 53 GeV for $p+p$, where the plateau only spans 3–4 rapidity units, and (b) the larger number of binary nucleon-nucleon collisions in heavy-ion reactions which will tend to make the $dE_T/d\eta$ distribution more focused around midrapidity.

The separate $dE_T/d\eta$ distributions for the electromagnetic and hadronic energy are shown in Fig. 10 for 200A GeV ^{32}S + ^{197}Au collisions. The distributions are seen to have approximately the same centroids and widths to within the errors. Consequently, the partition of electromagnetic and hadronic energy shows no obvious dependence on η. This is directly illustrated in Fig. 10(B), which shows the ratio $E_T^{\rm em}/E_T$ as a function of η. This ratio is essentially a constant to within the experimental errors. The EM energy is observed to be $\approx \frac{1}{4}$ of the total energy as noted earlier in the discussion of Fig. 5. If π^+, π^-, and π^0 are produced in equal abundance and photons from π^0 decay are assumed to be the only source of electromagnetic energy, then $\frac{1}{4}$ of the total E_T must arise from sources other than pions. Attempts to extract an estimate of the $dE_T/d\eta$ distribution of nucleons by assuming

$$\left.\frac{dE_T}{d\eta}\right|_{\rm nucleons} = \left.\frac{dE_T}{d\eta}\right|_{\rm total} - 3\left.\frac{dE_T}{d\eta}\right|_{\rm em} \qquad (21)$$

proved to be too unreliable.

The behavior of the quantities $dE_T/d\eta|_{\rm max}$, $\overline{\eta}$, and σ_η from Tables III–V are illustrated in Figs. 11–13. In the following this behavior will be discussed within the participant model described in Sections IV and VII.

Figure 11 shows the $dE_T/d\eta|_{\rm max}$ values from Table III plotted as a function of the total number of participants $\overline{W}$. In accordance with an earlier observation by WA80 [33], $dE_T/d\eta|_{\rm max}$ is approximately linearly proportional to the average number of participants $\overline{W}$ with the coefficient of proportionality equal to 0.64 and 0.90 GeV/nucleon at 60A and 200A, respectively. The increase of $dE_T/d\eta|_{\rm max}$ in Figs. 6 and 7 as a function of decreasing impact parameter or increasing target mass is therefore a simple consequence of the increase of $\overline{W}$.

The variation of the centroid $\overline{\eta}$ is more complicated. As can be seen from Table IV $\overline{\eta}$ will move backwards for increasing centrality, increasing target mass, decreasing projectile mass, or decreasing bombarding energy. All of these variations can be understood from the following approximate formula for the effective cm rapidity, $y_{\rm c.m.}$:

$$\overline{\eta} \approx y_{\rm c.m.} \approx \frac{1}{2}\left(y_p + y_t + ln\frac{W_p}{W_t}\right) . \qquad (22)$$

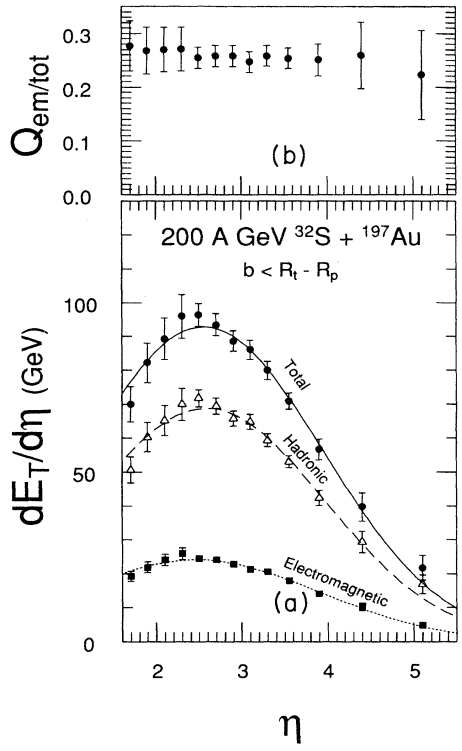

FIG. 10. (a) $dE_T/d\eta$ distributions for total, hadronic, and electromagnetic energy for 200A GeV ^{32}S + ^{197}Au central collisions. (b) Ratio $Q_{em/tot}$ between electromagnetic- and total $dE_T/d\eta$ distributions. See Fig. 6 for further details.

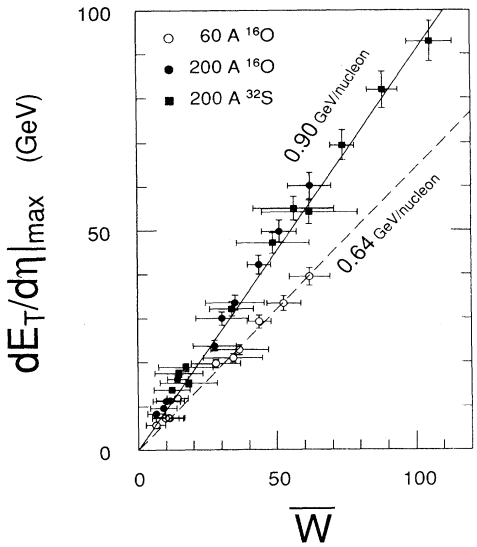

FIG. 11. Maximum value of the $dE_T/d\eta$ distributions as a function of the total average number of participants $\overline{W}$. The ordinates of the datapoints correspond to the values in Table III. The abscissas are calculated from (16) and (17) with the average performed over the impact parameter. The straight lines show linear fits through the origin to the data points at 60A GeV and 200A GeV, respectively.

y_p and y_t are the projectile and target rapidities, respectively. Equation (22) is based on the assumption that all of the W_p projectile participants interact collectively with all of the W_t target participants. Even if this is not the case, the above formula seems to qualitatively predict the correct behaviour of $\overline{\eta}$ as can be seen from the dotted line in Fig. 12. For decreasing impact parameter in an asymmetric projectile-target combination ($A_p < A_t$) the ratio W_p/W_t will decrease from ≈ 1 to $\approx \sqrt{A_p/A_t}$ for the most central collisions. This will, according to Eq. (22), cause $\overline{\eta}$ to decrease as observed in the data. Similarly, an increasing target mass or decreasing projectile mass will cause $\ln(W_p/W_T)$ to decrease, and finally an increase in $\sqrt{s}$ will increase $y_p + y_t$ causing $\overline{\eta}$ to increase as also observed in the data. It is, however, clear from observing the slope of the dotted line in Fig. 12 that Eq. (22) is not able to quantitatively predict the correct behavior, especially for heavy targets where the experimental centroids are situated at smaller rapidities than predicted by Eq. (22). A possible explanation for this deviation could be the increased importance of rescattering effects for heavy targets, which will tend to make the effective number of target participants larger and thereby move the effective center of mass backwards as observed in the data.

The width of the $dE_T/d\eta$ distributions, as shown in Fig. 13 and Table V, becomes narrower for more central collisions. This behavior is most likely caused by an increase in stopping, since the participants have to penetrate more nuclear matter in central collisions causing

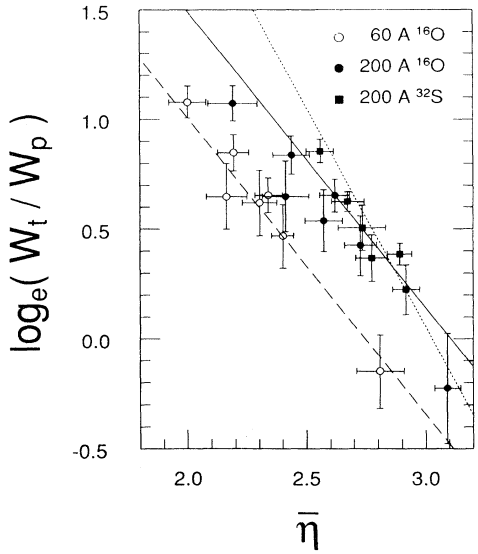

FIG. 12. Centroid $\overline{\eta}$ as a function of the ratio between target and projectile participants. The abscissas and ordinates of the data points have been obtained in a procedure similar to Fig. 11 except that the peripheral event class has been omitted since the very large vertical error bars for these data would make the figure too difficult to read. The dotted line shows the expected behavior at 200A GeV based on equation (22). The solid and dashed lines show the linear fits from equation (28) for 200A GeV and 60A GeV, respectively.

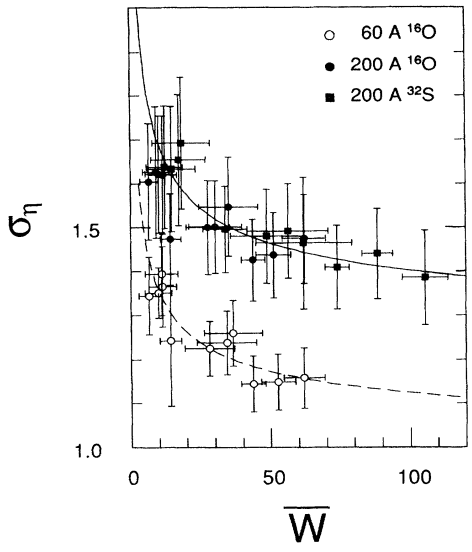

FIG. 13. Standard deviation σ_η the $dE_T/d\eta$ distributions as a function of the total number of participants. The abscissas and ordinates of the data points have been obtained in a procedure similar to Fig. 11. The solid and dashed lines show the fits from equation (28) for 200A GeV and 60A GeV, respectively.

them to have final rapidities closer to that of the effective center-of-mass system and causing a larger fraction of the produced particles to be emitted near midrapidity.

IX. PARAMETRIZATION OF $dE_T/d\eta$

Recently, substantial interest has been devoted to the mass and energy scaling of the E_T and $dE_T/d\eta$ distributions [9,34–36]. Universal scaling laws have been difficult to obtain as long as the scaling variables have been chosen as the projectile and target masses, A_p and A_t. In particular, most descriptions have been asymmetric in their target and projectile mass dependence, which seems unsatisfactory. As a continuation of our previous work [4], where WA80 has stressed the importance of incorporating the number of participant nucleons in a consistent description of high-energy nuclear collisions, we present below two universal parametrizations of the $dE_T/d\eta$ distributions. Instead of using the total masses A_p and A_t the key ingredient in these parametrizations is the use of the average number of projectile and target participants $\overline{W}_p$ and $\overline{W}_t$ for the impact parameter interval corresponding to the particular event class of the $dE_T/d\eta$ distribution. Once these participant variables have been chosen, a symmetric description between projectile and target can easily be obtained.

The first parametrization, given in Eqs. (24) and (25), is based on the observation that the $dE_T/d\eta$ distributions for a particular η value scales as a power law in both $\overline{W}_p$ and $\overline{W}_t$. The second parametrization, given in Eqs. (27) and (28), is based on the observation that the $dE_T/d\eta$ distributions, within WA80's η coverage of $1.6 < \eta < 5.5$, can be approximated very closely by Gaussian shapes.

The functional expression for the first parametrization of $dE_T/d\eta$ is

$$\frac{dE_T}{d\eta}(b) = G(\eta)\overline{W}_p^{\alpha(y_p-\eta)}\,\overline{W}_t^{\alpha(\eta-y_t)}\,, \tag{23}$$

$$\alpha(x) = \left[1+\exp\left(\frac{x-\eta_0}{\sigma_\alpha}\right)\right]^{-1}\,,$$

$$G(\eta) = \frac{N}{\sqrt{2\pi\sigma_n^2}}\,\exp\left[-\frac{1}{2}\left(\frac{\eta-\eta_0}{\sigma_n}\right)^2\right]\,. \tag{24}$$

$G(\eta)$ can be interpreted as a Gaussian describing the $dE_T/d\eta$ distribution for nucleon-nucleon collisions. $\overline{W}^\alpha$ describes the projectile and target mass dependence. The mass-dependence exponent α has been chosen as a Fermi distribution so $dE_T/d\eta$ scales with the number of target participants in the target rapidity region and is independent of the target in the projectile rapidity region. The projectile dependence is the inverse of this. This behavior can be directly observed in Fig. 14, which shows the experimental dependence of α as a function of η. Note that the A_t and A_p dependence in Figs. 14(A) and 14(B) is not symmetric since α for A_t^α only reaches 0.6 in the target rapidity region, whereas for A_p^α α reaches 1.0 in the projectile rapidity region. However, by expressing the power law dependence in terms of $\overline{W}_t$ and $\overline{W}_p$ an approximately symmetric dependence can be obtained as seen in Figs. 14(C) and 14(D). For the target dependence α now varies from 0.9 in the target rapidity region to close to zero in the projectile-rapidity region. The projectile dependence is similar.

The advantage of this parametrization is that it directly relates the $dE_T/d\eta$ distributions to a physically relevant set of quantities, the participants, and that it has a fairly high accuracy obtained with only 5 free parameters. The symmetric dependence on $\overline{W}_t$ and $\overline{W}_p$ furthermore enables a general parametrization to be constructed for all projectile and target combinations, whereas parametrizations based directly on the projectile and target masses will be applicable only to special cases. A drawback is the need to calculate the number of participants, which requires information on the impact parameter interval relevant for the particular $dE_T/d\eta$ distribution.

The parameters N, η_0, σ_n, and σ_α are found from least-squares fitting to the available WA80 data to be

$$N = 0.41\ (y_p - y_t - 1.51)\ \text{GeV}\,,$$

$$\eta_0 = 0.51\ (y_p + y_t)\,,$$

$$\sigma_n = 0.24\ (y_p - y_t)\,, \tag{25}$$

$$\sigma_\alpha = 0.12\ (y_p - y_t)\,.$$

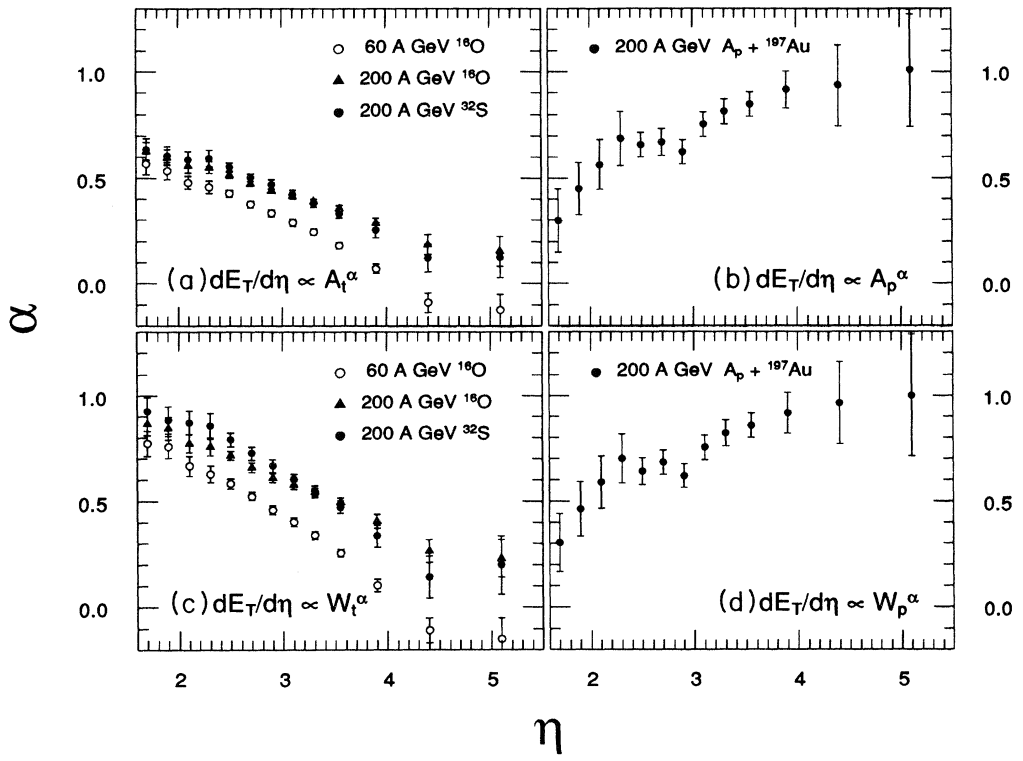

FIG. 14. Dependence of $dE_T/d\eta$ for $1.6 < \eta < 5.5$ on (a) target mass A_t, (b) projectile mass A_p, (c) target participants $\overline{W}_t$, and (d) projectile participants $\overline{W}_p$. The ordinate α is determined from a χ^2 fit to the available WA80 data by assuming a power-law dependence of $dE_T/d\eta$, i.e., $dE_T/d\eta \propto X^\alpha$ with $X = A_t$, A_p, $\overline{W}_t$, or $\overline{W}_p$. Note that the dependence on participants W is symmetric between projectile and target in contrast to the dependence on mass A.

y_p and y_t are the projectile and target rapidities, respectively. The 5 numerical values represent the 5 free parameters used in the least-square fitting.

The tested limits of applicability of this and the following parametrization are

$$16 \leq A_p \leq 32 \ ,$$

$$12 \leq A_t \leq 197 \ , \tag{26}$$

$$10 \leq \sqrt{s} \leq 20 \text{ GeV} \ ,$$

$$1.6 \leq \eta \leq 5.5 \ .$$

Within these limits the accuracy is better than 10% for 95% of the fitted data points. Figure 15(a) shows a set of typical comparisons between the parametrization and the experimental data.

As stated earlier the shapes of the experimental $dE_T/d\eta$ distributions are, to a very good approximation, Gaussian within the η interval of $1.6 < \eta < 5.5$ covered by WA80. Since a Gaussian distribution is characterized by its height, centroid, and standard deviation, it is a natural starting point for an alternative parametrization of $dE_T/d\eta$ to parameterize these three quantities. Several different functional forms have been tested and the following gave the smallest χ^2 with the use of 7 free variables:

$$\frac{dE_T}{d\eta}(b) = H \exp\left[-\frac{1}{2}\left(\frac{\eta - \eta_0}{\sigma_\eta}\right)^2\right] , \tag{27}$$

where the parameters are given by

$$H = 0.22\ (y_p - y_t - 1.94)\overline{W} \text{ GeV} \ ,$$

$$\eta_0 = 0.74\ \ln\frac{\overline{W}_p}{\overline{W}_t} + 0.30\ (y_p + y_t + 4.3) \ , \tag{28}$$

$$\sigma_\eta = 0.20\ (y_p - y_t)\ (1 + \overline{W}^{-0.36}) .$$

The choice of the functional expressions in (28) has been guided by the observations of the behaviour of the three Gaussian parameters in Figs. 11–13. The dashed and solid lines in these three figures show the predictions of (28) at $60A$ GeV and $200A$ GeV, respectively. Figure 15(b) shows the results of parametrization 2 for the same set of data as Fig. 15(a). The accuracy and limits of applicability of the parametrization in (27) and (28) are similar to these in the parametrization given in (24) and (25).

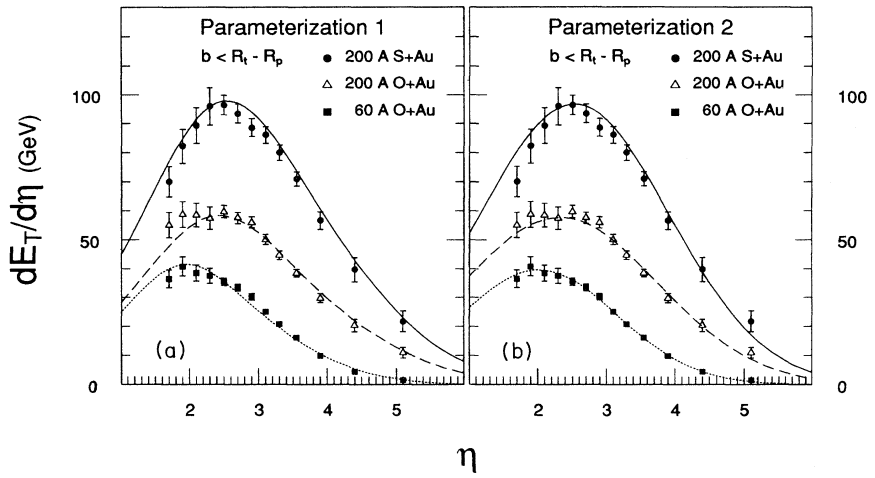

FIG. 15. A comparison between $dE_T/d\eta$ spectra (symbols with error bars) for ^{197}Au targets and (a) the parametrization 1 defined in (24) and (25) and (b) the parametrization 2 defined in (27) and (28).

X. NUCLEAR STOPPING POWER

Universally accepted estimates of the nuclear stopping power in heavy ion collisions have been difficult to obtain due to a proliferation of definitions of the concept. WA80 [4] and NA34 [5] have advocated the use of the "total E_T production ratio" R_t defined as the ratio between the experimentally measured total $E_T^{\rm tot}$ integrated over the full η range and the maximum transverse energy E_T^f in the isotropic fireball model:

$$R_t \equiv \frac{E_T^{\rm tot}}{E_T^f} ,$$

$$E_T^{\rm tot} = \int_{-\infty}^{\infty} \left.\frac{dE_T}{d\eta}\right|_{\rm data} d\eta , \qquad (29)$$

$$E_T^f = \frac{\pi}{4} \left(E_{\rm c.m.} - \overline{W} m_N\right) ,$$

where m_N is the nucleon mass. The use of the isotropic fireball model to evaluate the maximum E_T does not indicate that we consider this model a realistic description of high-energy nuclear collisions. On the contrary, it can be seen from our results presented below that this model is quite unsatisfactory. It is used here because the values of E_T^f and $dE_T^f/d\eta|_{\rm max}$ calculated in this model establish a natural scale for the E_t production, to which it has become common practice to compare the observed values of E_t [5, 8, 27, 28].

In most cases some kind of extrapolation is needed in order to evaluate $dE_T/d\eta\,|_{\rm data}$ in regions of η with no calorimeter coverage, which naturally introduces a degree of uncertainty in this procedure. In Table VI are shown our results for R_t, where $E_T^{\rm tot}$ has been obtained by integrating the Gaussian fits to the $dE_T/d\eta$ distributions. In no case is R_t close to unity, indicating that the E_T production is below the isotropic fireball limit. At 200A GeV R_t decreases from values around 0.50–0.60 in central collisions to values around 0.30–0.40 in peripheral collisions. For central collisions R_t is only slightly higher at 60A GeV than at 200A GeV. These dependences are naturally expected for a reasonable measure of stopping. ^{16}O-induced reactions show larger values of R_t than ^{32}S-induced for central collisions. This is probably because the relative abundance of participants only experiencing one or two binary nucleon-nucleon collisions increases when the colliding nuclei become more similar

TABLE VI. The total E_T production ratio R_t defined in (29) as the ratio between the measured total E_T and the total E_T in the isotropic fireball model.

	Total E_T production ratio R_t		
Target	60A ^{16}O	200A ^{16}O	200A ^{32}S
	Central		
Cu	0.57 ± 0.05	0.51 ± 0.05	0.48 ± 0.04
Ag	0.59 ± 0.06	0.54 ± 0.05	0.50 ± 0.04
Au	0.61 ± 0.05	0.59 ± 0.07	0.49 ± 0.04
	Intermediate		
C	0.52 ± 0.11	0.42 ± 0.06	
Al			0.38 ± 0.06
Cu	0.53 ± 0.11	0.40 ± 0.09	0.44 ± 0.07
Ag	0.52 ± 0.11	0.49 ± 0.11	0.46 ± 0.10
Au	0.54 ± 0.10	0.52 ± 0.12	0.40 ± 0.08
	Peripheral		
C	0.42 ± 0.13	0.39 ± 0.12	
Al			0.34 ± 0.12
Cu	0.41 ± 0.16	0.35 ± 0.14	0.37 ± 0.14
Ag	0.39 ± 0.17	0.37 ± 0.14	0.38 ± 0.13
Au	0.34 ± 0.10	0.35 ± 0.13	0.27 ± 0.09

TABLE VII. The midrapidity E_T production ratio R_m defined in (30) as the ratio between the measured $dE_T/d\eta|_{\max}$ and $dE_T/d\eta|_{\max}$ in the isotropic fireball model.

	Mid-rapidity E_T Production Ratio R_m		
Target	60A ^{16}O	200A ^{16}O	200A ^{32}S
	Central		
Cu	0.31 ± 0.03	0.22 ± 0.02	0.21 ± 0.01
Ag	0.32 ± 0.03	0.24 ± 0.02	0.22 ± 0.01
Au	0.33 ± 0.02	0.25 ± 0.02	0.22 ± 0.01
	Intermediate		
C	0.26 ± 0.05	0.18 ± 0.02	
Al			0.16 ± 0.02
Cu	0.27 ± 0.05	0.17 ± 0.03	0.19 ± 0.03
Ag	0.26 ± 0.06	0.20 ± 0.05	0.19 ± 0.04
Au	0.27 ± 0.05	0.21 ± 0.05	0.17 ± 0.03
	Peripheral		
C	0.20 ± 0.06	0.15 ± 0.05	
Al			0.13 ± 0.04
Cu	0.19 ± 0.07	0.14 ± 0.05	0.14 ± 0.05
Ag	0.18 ± 0.08	0.14 ± 0.05	0.15 ± 0.05
Au	0.15 ± 0.04	0.13 ± 0.05	0.10 ± 0.03

in size, which will reduce the relative amount of the total CM energy transferred into transverse energy.

Another measure of stopping, introduced by WA80 [4], has been the "midrapidity E_T production ratio" R_m, defined as

$$R_m \equiv \frac{dE_T^{\text{data}}/d\eta|_{\max}}{dE_T^f/d\eta|_{\max}}$$

$$dE_T^f/d\eta|_{\max} = \frac{1}{2}\,(E_{\text{c.m.}} - \overline{W} m_N)\ , \tag{30}$$

where $dE_T^f/d\eta|_{\max}$ is the maximum value of $dE_T/d\eta$ in the isotropic fireball model. This measure is easy and reliable to calculate. The results for R_m are shown in Table VII. Note that R_m behaves qualitatively similar to R_t, but quantitatively the variations are more pronounced. If the isotropic fireball model is assumed to correspond to the highest attainable amount of stopping, then $dE_T^f/d\eta|_{\max}$ is directly related to the highest attainable energy density within the Bjorken picture [see Eq. (31)]. Based on this, R_m can then be interpreted as the ratio between the attained energy density and the highest possible energy density.

XI. ENERGY DENSITY ESTIMATE

It has been customary to extract values of the energy density reached in high-energy nuclear collisions from the measured values of either E_T or $dE_T/d\eta$. A frequently employed method is based on a formula by Bjorken [32]

$$\varepsilon_{\text{BJ}} = \frac{dE_T/d\eta|_{\max}}{\pi R_0^2 \tau_0}\ , \tag{31}$$

where πR_0^2 is the transverse area of the smaller of the colliding nuclei and τ_0 is the formation time, which usually is assumed to have a value close to 1 fm/c. Table VIII shows the results for ε_{BJ} obtained in central collisions. The radii of ^{16}O and ^{32}S have been calculated in the sharp sphere approximation with $r_0 = 1.2$ fm and the formation time has been given its canonical value $\tau_0 = 1$ fm/c. The energy density increases as a function of both bombarding energy and target mass whereas it is found to be independent of projectile mass. A maximum value of ≈ 2 GeV/fm^3 is reached in 200A GeV ^{16}O + ^{197}Au and ^{32}S + ^{197}Au central collisions. It should be noted that these dependences most likely will only apply to situations where the projectile is much smaller than the target. The values of the energy densities shown in Table VIII are averaged over all central collisions. Higher estimates of the energy density can be obtained by selecting a smaller sample of events with larger values of $dE_T/d\eta|_{\max}$. For ^{32}S + ^{197}Au the largest observed value of $dE_T/d\eta|_{\max}$ was 130 GeV which implies $\varepsilon_{\text{BJ}} = 2.9$ GeV/fm^3. The corresponding cross section was ≈ 1 μb.

The use of this relation has several advantages. It uses an easily accessible experimental quantity $dE_T/d\eta|_{\max}$. Disagreements over the correct value of τ_0 can take the form of a simple rescaling. A further advantage is that it does not consider E_T produced at one proper time and a reaction volume at another proper time, as do several approaches for estimating energy densities based on the global E_T.

The use of Bjorken's formula has several disadvantages. The most important is that it leads to overestimates of ε since it does not take the finite nuclear collision times into account. At 200A GeV this time is of the order of 1.2 fm/c, which is comparable to the formation time. This will lead to a slower buildup of energy density than assumed in Bjorken's approach. Another important objection to (31) is that it is derived from the assumption of longitudinal rapidity scaling which, as described in Section VIII, is not supported by the data at SPS energies. More realistic methods for estimating the attained energy densities from experimental data are therefore urgently needed.

TABLE VIII. Energy densities in central collisions obtained by Bjorken's formula. The error bars reflect only the experimental error in $dE_T/d\eta|_{\max}$, not any systematic error originating from uncertainties in estimating the reaction volume.

	ε_{BJ} (GeV/fm^3)		
Target	60A ^{16}O	200A ^{16}O	200A ^{32}S
	central		
Cu	1.0 ± 0.1	1.5 ± 0.1	1.5 ± 0.1
Ag	1.2 ± 0.1	1.8 ± 0.1	1.8 ± 0.1
Au	1.4 ± 0.1	2.1 ± 0.1	2.0 ± 0.1

XII. SUMMARY AND CONCLUSIONS

Distributions of transverse energy for $2.4 < \eta < 5.5$, forward energy for $\eta > 6.0$, and $dE_T/d\eta$ distributions for $1.6 < \eta < 5.5$ have been presented for 60A GeV and 200A GeV ^{16}O-induced and 200A GeV ^{32}S-induced reactions on five nuclear targets. The transverse energy information was extracted from the midrapidity calorimeter with a novel technique that compensated for the response of the calorimeter and allowed a separation of the event energy into its electromagnetic and hadronic components. The shapes of the forward energy spectra were strongly influenced by the nuclear overlap geometry and scaled approximately with the ratio between the radii of the colliding nuclei. The transverse energy showed a strong target dependence at 200A GeV and no target dependence for the heavier targets at 60A GeV. This lack of target dependence at the low bombarding energy was not interpreted as evidence of full nuclear stopping, but as a kinematical effect caused by the WA80 calorimeter η coverage being limited to the forward center-of-mass hemisphere. The approximate constancy of the ratio of electromagnetic E_T to total E_T at 200A GeV made it possible to estimate the upper limit for the p_T-integrated direct photon production to be 20% of the π^0 yield. A limit as low as 10% could be obtained if the average energies of direct photons and π^0's were identical. These estimates correlate well with the value of 15% extracted from the WA80 SAPHIR detector with fewer assumptions.

Based on the assumption that the forward energy varied monotonically with the impact parameter and using Glauber theory the average number of projectile and target participants could be extracted for various event classes. This information was used in the interpretation of the $dE_T/d\eta$ distributions. The information content of each of these distributions corresponded to a Gaussian fit with 3 free parameters: the height $dE_T/d\eta|_{\max}$, the centroid $\overline{\eta}$, and the standard deviation σ_η. $dE_T/d\eta|_{\max}$ was found to depend linearly on the average total number of participants with coefficients of proportionality of 0.64 and 0.90 GeV/nucleon at 60A GeV and 200A GeV, respectively. $\overline{\eta}$ was found to increase linearly with both the beam rapidity and the logarithm of the ratio between the number of projectile and target participants. Finally, σ_η was found to increase with beam rapidity and decrease with the total number of participants.

The use of projectile and target participants instead of projectile and target masses allowed the construction of two universal parametrizations of the $dE_T/d\eta$ distributions. The first parametrization was based on the observation that the $dE_T/d\eta$ distributions for a given η interval scaled as a power law in the number of both the projectile and target participants. The second parametrization was based on a parametrization of the three Gaussian parameters described in the previous paragraph. The experimental results for two different measures of nuclear stopping, the "total E_T production ratio" and the "midrapidity E_T production ratio," were presented for three different centrality cuts for all measured projectile-target combinations. Both measures increased as a function of centrality and as a function of target mass for central collisions and decreased as a function of bombarding energy. Finally estimates of the attained energy densities based on Bjorken's formula were presented. A mean value of ≈ 2 GeV/fm^3 was found in 200A GeV ^{16}O + ^{197}Au and ^{32}S + ^{197}Au central collisions. For the most violent ^{32}S + ^{197}Au reactions a value of ≈ 2.9 GeV/fm^3 was reached at the 1 μb level.

ACKNOWLEDGMENTS

We appreciate the excellent work of the accelerator divisions of CERN, GSI, and LBL which has resulted in the development and delivery of the ^{16}O and ^{32}S beams used in this work. Partial support by the German BFMT and DFG, the U.S. DOE, the Swedish NFR, the Humbolt Foundation and the CERN-PPE Division is gratefully acknowledged.

* Present address: CERN PPE, Geneva, Switzerland.
† Present address: KVI, University of Groningen, Groningen, The Netherlands.
‡ Present address: The Institute for Nuclear Studies, Warsaw, Poland.
§ Present address: Purdue University, West Lafayette, IN 47907.

[1] The proceedings from the most recent quark matter conferences provide an excellent introduction to the field: *Quark Matter 90*, Proceedings, Menton, France [Nucl. Phys. **A525**, 1c (1991)]; *Quark Matter 89*, Proceedings, Lenox [Nucl. Phys. **A498**, 1c (1989)]; *Quark Matter 87*, Proceedings, Nordkirchen, Germany [Z. Phys. C **38**, 1 (1988)].
[2] NA35 Collaboration, A. Bamberger *et al.*, Phys. Lett. B **184**, 271 (1987).
[3] E802 Collaboration, T. Abbott *et al.*, Phys. Lett. B **197**, 285 (1987).
[4] WA80, Collaboration, R. Albrecht *et al.*, Phys. Lett. B **199**, 297 (1987).
[5] NA34 Collaboration, T. Åkesson *et al.*, Z. Phys. C **38**, 383 (1988).
[6] NA34 Collaboration, T. Åkesson *et al.*, Phys. Lett. B **214**, 295 (1988).
[7] E814 Collaboration, J. Barrette *et al.*, Phys. Rev. Lett. **64**, 1219 (1990).
[8] M. J. Tannenbaum, Int. J. Mod. Phys. A **4**, 3377 (1989).
[9] J. Stachel, Nucl. Phys. **A525**, 23 (1991).
[10] WA80, R. Albrecht *et al.*, Report No. GSI-85-32, Collaboration Gesellschaft für Schwerionenforschung, D-6100 Darmstadt, 1985.
[11] T. C. Awes *et al.*, Nucl. Instrum. Methods A **279**, 479 (1989).
[12] G. R. Young *et al.*, Nucl. Instrum. Methods **A279**, 503 (1989).
[13] B. Anderson, G. Gustafson and B. Nilsson-Almqvist, Nucl. Phys. **B281**, 289 (1987); B. Nilsson-Almqvist and E. Stenlund, Comput. Phys. Commun. **43**, 387 (1987).

[14] K. Werner, Phys.Lett. **B208**, 520 (1988); K. Werner. Phys. Rev. Lett. **62**, 2460 (1989); K. Werner, Z. Phys. C **42**, 85 (1989); K. Werner and P. Koch, Phys. Lett. **B242**, 251 (1990).
[15] A. Shor and S. Longacre, Phys. Lett. B **218**, 100 (1989).
[16] A computer file containing all data points of the spectra published in this paper can be obtained by contacting WA80 at the BITNET address: SORENSEN@UTKVX.
[17] R. J. Glauber, in *Lectures in Theoretical Physics*, edited by W. E. Brittin and L. G. Durham (Interscience, New York, 1959), Vol. 1, p. 315.
[18] C.-Y. Wong, Phys. Rev. D **30**, 972 (1984).
[19] C.-Y. Wong, Phys. Rev. D **32**, 94 (1985).
[20] C.-Y. Wong and Z.-D. Lu, Phys. Rev. D **39**, 2606 (1989).
[21] H. De Vries, C. W. De Jager, and C. De Vries, At. Data Nucl. Data Tables, **36** 495 (1987).
[22] H. L. Bradt and B. Peters, Phys. Rev. **77**, 54 (1950).
[23] P. J. Karol, Phys. Rev. C **11**, 1203 (1975).
[24] H. H. Heckman, D. E. Greiner, P. J. Lindstrom, and H. Shwe, Phys. Rev. C **17**, 1735 (1978).
[25] WA80 Collaboration, R. Albrecht *et al.*, Z. Phys. C **45**, 31 (1989).
[26] J. Stachel and P. Braun-Munzinger, Phys. Lett. B **216**, 1 (1989).
[27] Helios Collaboration, T. Akesson *et al.*, Nucl. Phys. **B353**, 1 (1991).
[28] NA35 Collaboration, J. Bachler *et al.*, Report No. IKF91-1 (submitted to Z. Phys. C).
[29] C. M. G. Lattes, Phys. Rep. **65**, 151 (1980).
[30] F. Halzen and H. C. Liu, Phys. Rev. D **25**, 1842 (1982).
[31] WA80 Collaboration, Z. Phys. C (to be published).
[32] J. D. Bjorken, Phys. Rev. D **27**, 140 (1983).
[33] WA80 Collaboration, S. P. Sorensen *et al.*, Z. Phys. C **38**, 3 (1988).
[34] WA80 Collaboration, G. R. Young *et al.*, Nucl. Phys. **A498**, 53c (1989).
[35] HELIOS Collaboration, J. Schukraft *et al.*, Nucl. Phys. **A498**, 79c (1989).
[36] NA35 Collaboration, J Harris *et al.*, Nucl. Phys. **A498**, 133c (1989).